Published in final edited form as:
IEEE Trans Inf Technol Biomed. 2012 September ; 16(5): 842–851. doi:10.1109/TITB.2012.2204405.

A Framework of Whole Heart Extracellular Volume Fraction Estimation for Low Dose Cardiac CT Images

Xinjian Chen, **Marcelo Souto Nacif**, **Songtao Liu**, **Christopher Sibley**, **Ronald M. Summers**, **David A. Bluemke**, and **Jianhua Yao**
Radiology and Imaging Sciences Department, National Institutes of Health Clinical Center, Bethesda, MD 20892-1182, USA, Ph: (301)594-8139, Fax:(301)480-9827

Abstract

Cardiac CT (CCT) is widely available and has been validated for detection of focal myocardial scar using delayed enhancement technique. CCT however has not been previously evaluated for quantification of diffuse myocardial fibrosis. In our investigation, we sought to evaluate the potential of low dose CCT for the measurement of myocardial whole heart extracellular volume (ECV) fraction. ECV is altered in conditions of increased myocardial fibrosis. A framework consisting of three main steps was proposed for CCT whole heart ECV estimation. First, a shape constrained graph cut (GC) method was proposed for myocardium and blood pool segmentation on post-contrast image. Second, the symmetric Demons deformable registration method was applied to register pre-contrast to post-contrast images. So the correspondences between the voxels from pre-contrast to post-contrast images were established. Finally, the whole heart ECV value was computed. The proposed method was tested on 20 clinical low dose CCT datasets with pre-contrast and post-contrast images. The preliminary results demonstrated the feasibility and efficiency of the proposed method.

Keywords

Cardiac CT; Myocardium Segmentation; Registration; Extracellular Volume Fraction

I. INTRODUCTION

Diffuse myocardial fibrosis is an increasingly recognized pathologic endpoint that is observed in association with a variety of cardiomyopathies and heart failure. Myocardium extracellular volume fraction (ECV) is increased in association with diffuse myocardial fibrosis, a hallmark of pathologic remodeling [1]. Cardiac magnetic resonance imaging (CMRI) has been well validated and allows quantification of myocardial fibrosis in comparison to overall mass of the myocardium [2]. CMRI T1 mapping with ECV determination [3, 4] is a novel method to quantify diffuse fibrosis non-invasive, and has been validated in multiple conditions, including myocardial infarction, heart failure, aortic regurgitation, and cardiomyopathy. Unfortunately, CMRI is relatively expensive, time consuming and contraindicated in patients with intracardiac devices and irregular heart beat. In addition, claustrophobia is present in about 5% or more of CMRI subjects [5]. Cardiac CT (CCT) has emerged as a common and widespread technology and also has been validated for detection of focal myocardial scar [6] and myocardial stress/rest perfusion [7]. CCT acquisition is much faster but is less sensitive to contrast differences than CMRI. In this paper, we sought to evaluate the potential of low dose CCT for the measurement of myocardial 3D whole heart ECV fraction.

There are several investigations related with ECV fraction computation [3-5,8]. In all of these methods, the ECV fraction was computed based on multiple 2D regions of interest (ROI). However, the diffuse fibrosis is a global process and a whole heart ECV estimation is highly desirable for clinical application. In order to compute the 3D ECV fraction, pixel to pixel correspondence between the pre-contrast and post-contrast images need to be established. This can be accomplished by registration methods. Fig. 1 shows examples of pre-contrast and post-contrast CCT images. As we can see from the figure, it is nearly impossible to differentiate myocardium and blood pool in the pre-contrast image and the segmentation of myocardium and blood pool in post-contrast image is also a challenging task. For accurate 3D ECV fraction computation, advanced registration and segmentation methods are highly desired. A brief review of the related segmentation and registration methods is given below.

The segmentation of the cardiac images has been the motivation of many research works. The cardiac image segmentation methods [9] may be classified into several types: image based [9-15], model based [16-22], and hybrid methods [23-26]. Image based methods perform segmentation based on the image information available in the image; these include edge detection [10,11], active contours [12, 13], level set (LS) [14], fuzzy connectedness [15] and graph cut (GC) [16]. These methods perform well on high quality images. However, the results are not as good when the image quality is inferior or boundary information is missing. In recent years, there has been an increasing interest in model-based segmentation methods. One advantage of these methods is that, even when some boundary information is missing, such gaps can be filled due to the introduced prior knowledge present in the model. These models were based on different geometric and physical representations, including spring-mass models [17], triangle-based finite element models [18], simplex meshes [19], finite element models [20], 3D B-Spline deformation fields [21] and statistical shape and appearance models [22, 23, 24]. The hybrid approaches are rightfully attracting a great deal of attention at present. The synergy that exists between these two approaches –image-based and model-based strategies – is clearly emerging in the segmentation field. As such, hybrid methods that form a combination of two or more approaches are emerging as powerful segmentation tools where their superior performances and robustness over each of the components are beginning to be well demonstrated [25 , 26 , 27 , 28]. In this paper, the cardiac segmentation is based on an advanced hybrid method which effectively integrates the GC method with the shape information computed from the LW method . There are several shape prior integrated segmentation methods have been proposed, such as shape prior integrated LS methods [29, 30], shape prior integrated GC methods [27, 28].The LS method has been widely used, however, it is not trivial to construct appropriate velocities for advancing the LS function. We propose to apply the shape integrated GC method to take advantage that the GC method can compute the global optimum solution for the two-label segmentation and enforce piecewise smoothness [16]. The shape integrated GC methods further improve the GC by effectively combining the shape priors information. In this paper, the shape prior information is computed via the LW method, which is a user-steered 2-dimensional segmentation method. During the process of LW segmentation, the user provides recognition help and the algorithm performs optimal delineation based on dynamic programming.

Image registration is not a trivial task and cardiac image registration is a more complex problem in particular because of the nonrigid and mixed motions of the heart and the thorax structures. Moreover, as compared to other organ's registration such as brain, the heart exhibits fewer accurate anatomical landmarks. Also, cardiac images are usually acquired with a lower resolution than brain images. The common used cardiac registration method could be classified into two main categories: 1) those based on geometric image features [27-29] and those based on voxel similarity measures [30-38]. The geometric image feature-

based methods are divided into registration of a set of points [31] and edges or surfaces [32, 33]. Registration methods based on voxel similarity measures include moments and principal-axes methods [34, 35], intensity difference and correlation methods [36, 37], atlas based method [38] and methods based on mutual information [39, 40]. The Demons algorithm [41] is a well-established technique for non-rigid registration. One of the most efficient methods is the demons algorithm proposed by Thirion [42]. Several variants of the algorithm have been proposed depending on how the forces are computed, such as an adhoc symmetrization of the demons force [43], and symmetric forces [44]. Vercauteren et al. [45] explained from a theoretical point of view that the symmetric forces demons algorithm is more efficient in practice. In this paper, the symmetric demons deformable registration method is applied for the registration due to its efficiency.

In this paper, we propose a novel framework for 3D whole heart ECV fraction estimation on low dose CCT images. The proposed framework consists of three main steps. First, a hybrid segmentation method is proposed for myocardium and blood pool segmentation on post-contrast image. The hybrid method contains two steps: initialization and segmentation. A pseudo-3D strategy is applied for the initialization based on the live wire (LW) method [39]. Then the shape information generated from the initialization step is integrated into the GC cost function, and this shape prior integrated GC is applied for the finer segmentation. Second, the symmetric Demons [**Error! Bookmark not defined.**37] deformable registration method is applied to register pre-contrast to post-contrast images. So the correspondences between the voxels from pre-contrast to post-contrast images were established. Finally, the whole heart ECV value was computed. Our contributions in this paper are summarized as follows,

1. To the best of our knowledge, we are the first one to propose a framework of 3D whole heart ECV estimation using low dose cardiac CT Images.
2. For the myocardium and blood pool segmentation, we propose an advanced segmentation method which integrates the shape prior information generated from the LW method with the GC method.
3. For the registration of pre-contrast and post-contrast image, we apply the symmetric Demons method.

The rest of the paper is organized as follows. In Section 2, we elaborate the complete methodology of the 3D whole heart ECV fraction computation. In Section 3, we evaluate the performance of the proposed method. In Section 4, we provide discussions and conclusions.

II. METHOD AND MATERIALS

A flowchart of the proposed method is shown in Fig. 2. The proposed framework consists of three main steps: shape constrained GC based segmentation, symmetric Demons based registration and ECV computation. Among these three steps, the segmentation and registration are the core part of the proposed framework. The details are given in the each sub-section as below.

2.1 Myocardium and Blood Pool Segmentation Based on a Shape Constrained GC Method

The proposed segmentation method consists of two main steps. First, the cardiac contour is initialized by segmenting the top, middle and bottom slices via live wire method [46], and then the contours in between are linearly interpolated. Second, the object shape information generated from the initialization step is integrated into the GC cost computation, and then this shape constrained GC is used for the myocardium and blood pool segmentation.

2.1.1 Initialization—The objective of the initialization is to generate the shape constraints for the latter GC segmentation. The initialization is consist of two steps: first, the cardiac contour is initialized by segmenting the top, middle and bottom slices via LW method, and then the contours in between are linearly interpolated so the 3D shape contour is generated. The LW segmentation is conducted on only three slices due to two reasons: (1) the LW is a user steered 2D segmentation method, i.e., it needs user input for the landmarks and is time consuming. (2) three slices are sufficient to generate the rough shape, which will be refined by the latter GC segmentation. During the process of LW segmenation, the user provides the landmarks on the boundary then the LW method will do the delineation automatically [46]. The user usually only need to provide about 10 landmarks per slice.

An oriented boundary cost function is devised for myocardium contour as per the *LW* method [46]. Following the original terminology and notation in [46], we define a *boundary element, bel* for short, as an oriented edge between two pixels. For a given image slice *I,* a *bel* will be represented as an ordered pair (*p, q*) of 4-adjacent pixels where *p* is inside the object (pixel value 1) and *q* is outside (pixel value 0). We think of every pixel edge of *I* as constituting two potential *bels* (*p, q*) and (*q, p*) and possibly assign different cost values to them. To every *bel* of *I,* we assign a set of features depending on the orientation (*p, q*) or (*q, p*). The features assigned to each *bel* are intended to express the likelihood of the *bel* belonging to the boundary of a particular object of interest. In our particular case, the cost $c(l)$ associated with *bel l* is a linear combination of the costs assigned to its features

$$c(l) = \frac{\sum_{i=1}^{nf} w_i c_f(f_i(l))}{\sum_{i=1}^{nf} w_i}, \quad (1)$$

where *nf* is the number of features, w_i is a positive constant indicating the emphasis given to feature f_i, and c_f is the function to convert feature values $f_i(l)$ at *l* to cost values $c_f(f_i(l))$. In LW [46], f_i may represent features such as intensity on the immediate interior of the boundary, intensity on the immediate exterior of the boundary, and gradient magnitude at the center of the *bel*. Depending on the intensity characteristics of the object of interest, different f_i may be combined. As suggested in [46], c_f is chosen as an inverted Gaussian function, and all selected features are combined with weights w_i. We utilize the feature of *LW* to define the best-oriented path between any two-landmark points (x_k and x_{k+1}) as a sequence of *bels* with minimum total cost:

$$\kappa(X_k, X_{k+1}) = \sum_{i=1}^{h} c(l_i), \quad (2)$$

where *h* represents the number of *bels* in the best-oriented path $<l_1, l_2, \ldots, l_h>$. The total cost structure $\mathcal{K}(\mathbf{x})$ associated with all the landmarks may now be defined as

$$\kappa(\mathbf{X}) = \sum_{k=1}^{m} \kappa(X_k, X_{k+1}), \quad (3)$$

where *m* is the number of landmarks for the object of interest and we assume that $x_{m+1} = x_1$ (closed contour). In other words, $\mathcal{K}(\mathbf{x})$ is the sum of the costs associated with the best oriented paths between all *m* pairs of successive landmarks of shape instance **x**. The parameters of $\mathcal{K}(\mathbf{x})$ for each object shape **x** are estimated automatically as described in [46] by using the training images.

2.1.2 Shape Constrained GC Method—We propose a shape-constrained GC method for the myocardium and blood pool segmentation. The proposed algorithm effectively integrates the shape information from initialization step with the optimal 3D delineation capability of the GC method.

GC segmentation can be formulated as an energy minimization problem such that for a set of pixels P and a set of labels L, the goal is to find a labeling $f: P \rightarrow L$ that minimizes the energy function $En(f)$.

$$En(f) = \sum_{p \in P} R_p(f_p) + \sum_{p \in P, q \in N_p} B_{p,q}(f_p, f_q), \quad (6)$$

where N_p is the set of pixels in the neighborhood of p, $R_p(f_p)$ is the cost of assigning label $f_p \in L$ to p, and $B_{p,q}(f_p, f_q)$ is the cost of assigning labels $f_p, f_q \in L$ to p and q. In two-class labeling, $L = \{0, 1\}$, the problem can be solved efficiently with graph cuts in polynomial time when $B_{p,q}$ is a sub-modular function, *i.e.*, $B_{p,q}(0, 0) + B_{p,q}(1, 1) \leq B_{p,q}(0, 1) + B_{p,q}(1, 0)$ [47].

In our framework, the unary cost $R_p(f_p)$ is the sum of a data penalty $D_p(f_p)$ and a shape penalty $S_p(f_p)$ term. The data term is defined based on image intensity and can be considered as a log likelihood of the image intensity for the target object. The shape prior term is independent of image information, and the boundary term is based on the gradient of the image intensity.

The proposed shape-integrated energy function is defined as follows:

$$En(f) = \sum_{p \in P} \left(\alpha \cdot D_p(f_p) + \beta \cdot S_p(f_p)\right) + \sum_{p \in P, q \in N_p} \gamma \cdot B_{p,q}(f_p, f_q), \quad (7)$$

where α, β, γ are the weights for the data term, shape term S_p, and boundary term, respectively, satisfying $\alpha + \beta + \gamma = 1$. These components are defined as follows:

$$D_p(f_p) = \begin{cases} -\ln P(I_p|O), & \text{if } f_p = \text{object label} \\ -\ln P(I_p|B), & \text{if } f_p = \text{background label} \end{cases} \quad (8)$$

$$B_{p,q}(f_p, f_q) = \exp\left(-\frac{(I_p - I_q)^2}{2\sigma^2}\right) \cdot \frac{1}{d(p,q)} \cdot \delta(f_p, f_q), \quad (9)$$

and

$$\delta(f_p, f_q) = \begin{cases} 1, & \text{if } f_p \neq f_q \\ 0, & \text{otherwise} \end{cases}, \quad (10)$$

where I_p is the intensity of pixel p; *object label* is the label of the object (foreground); $P(I_p|O)$ and $P(I_p|B)$ are the probability of intensity of pixel p belonging to object and background, respectively, which are estimated from object and background intensity histograms during the training phase (details given below); $d(p, q)$ is the Euclidian distance between pixels p and q; and σ is the standard deviation of the intensity differences of neighboring voxels along the boundary.

$$S_p\left(f_p\right)=1-\exp\left(-\frac{d\left(p,\mathbf{x}_o\right)}{r_o}\right) \quad (11)$$

where $d(p, \mathbf{x}_O)$ is the distance from pixel p to the set of pixels which constitute the interior of the current shape $\mathbf{x}_O$ of object O (note that if p is in the interior of $\mathbf{x}_O$, then $d(p, \mathbf{x}_O) = 0$); r_O is the radius of a circle that just encloses $\mathbf{x}_O$. The linear time method of reference [48] was used in this paper for computing this distance.

Minimizing *En* with Graph Cuts: The minimization of Eqn. (7) can be solved by *GC* method. The graph is designed as follows. We take $V = P \cup L$, *i.e.*, V contains all the pixel nodes and terminals corresponding to the labels in L which represent objects of interest plus the background. $A = A_N \cup A_T$, where A_N is the n-links which connect pixels p and q ($p \in P$, $q \in N_p$) and with a weight of $w_{p,q}$. A_T is the set of t-links which connect pixel p and terminals $L \in L$ and with a weight of $w_{p,\ell}$. The desired graph with cut cost $|C|$ equaling $En(f)$ is constructed using the following weight assignments:

$$w_{p,q}=\gamma \cdot B_{p,q}; \quad (12)$$

$$w_{p,\ell}=K-\left(\alpha \cdot D_p(\ell)+\beta \cdot S_p(\ell)\right); \quad (13)$$

where K is constant that is large enough to make the weights $w_{p,\ell}$ positive.

2.2 Deformable Registration by Symmetric Demons Algorithm

In order to compute the 3D ECV fraction, the pixel to pixel correspondence between the pre-contrast and post-contrast images must be established. In this paper, the symmetric deformable Demons registration method [] is applied. The Demons algorithm has been widely used for images registration field and achieved good results. Demons method is a non-parametric non-rigid image registration method. It alternates between computation of the optical flow forces and regularization by a Gaussian smoothing.

The Demons algorithm could be seen as an optimization of a global energy. The main idea is to introduce a hidden variable in the registration process: correspondences. We then consider the regularization criterion as a prior on the smoothness of the transformation. Instead of requiring that point correspondences between image pixels be exact realizations of the transformation, one allows some error at each image point. For the symmetric force demon registration, the modification was made to avoid large deformations when gradients have small values [45]. Vercauteren et al. [45] explained from a theoretical point of view that the symmetric force demon algorithm is more efficient in practice, which is the main reason to choose this technique in our system. We use the implementation contributed by Corinne Mattmann, ETH Zurich, Switzerland. The registration program was implemented using components of the open source segmentation and registration toolkits [49], which are cross-platform C++ software toolkits and are freely available from http://www.itk.org.

The influence of the standard deviation σ of the Gaussian kernel used during the demons registration process to the deformation field is studied. This parameter is related to the regularity of the estimated deformation field: the higher σ, the smoother the deformation field. And the influence of the number of iterations on the convergence of the algorithm and on the CPU time is also studied.

2.3 ECV Fraction Computation

After registration, the correspondences of the voxels between the pre-contrast and post-contrast images were established. Myocardial and blood pool Hounsfield unit attenuation values at each voxel were recorded and extracellular volume fraction was computed as follows,

$$\mathrm{ECV}=\left(\Delta\mathrm{HU}_{\mathrm{myocardium}}/\Delta\mathrm{HU}_{\mathrm{blood}}\right)^{*}\left(1-\mathrm{Hct}_{\mathrm{blood}}\right), \quad (14)$$

where Hct is the hematocrit, and ΔHU is the change in Hounsfield unit attenuation (ΔHU = $\mathrm{HU}_{\mathrm{post\ iodine}} - \mathrm{HU}_{\mathrm{pre\ iodine}}$).

III. EXPERIMENTAL RESULTS

The proposed methods were tested on a clinical CCT data set. This data set contained images of 20 subjects (10 heart failure subjects with 10 age and gender matched controls, ages 60.9 ± 7.2 (mean ± st.dev.)), acquired from the pre-contrast and post-contrast phases of 320-MDCT scanner (Aquilion One, Toshiba Medical Systems, Tustin, CA). The slice thickness is 3 mm and in-plane pixel size is 0.37*0.37 mm. The image size is 512*512*47.

3.1 Parameters Training

In this paper, the leave-one-out strategy is used for the evaluation. The parameters of LW and shape integrated GC methods are optimized through the training. We have 10 post-contrasted CCT images, i.e., when testing on one image, other 9 images will be used for training. The parameters of live wire method, such as number of features, weight for each feature are optimized through the training. For more details please see [46], and the executable version can be downloaded from http://www.mipg.upenn.edu/cavass/. The parameters of GC method are determined also through the training stage. The intensity histograms for each object are estimated from the training images. Based on this, $P(I_p \mid O)$ and $P(I_p \mid B)$ can be computed. As for parameters α, β and γ in Eqn. (7), since $\alpha + \beta + \gamma = 1$, we estimate only α and β by optimizing accuracy as a function of α and β and set $\gamma = 1-\alpha-\beta$. We use the gradient descent method for the optimization. Let $Accu(\alpha, \beta)$ represent the algorithm's accuracy (here we use the true positive volume fraction [50]), α and β are initialized to 0.35 each, then $Accu(\alpha, \beta)$ is optimized over the training data set to determine the best α and β.

3.2 Evaluation of the Segmentation Method

An expert in CCT imaging field manually segmented the post-contrast cardiac images and the results were used as the references for the segmentation evaluation. Fig. 3 shows the myocardium and blood pool segmentation results on three slices. From visual checking, we can find the results are quite good.

The quantitative evaluation of the proposed approach results are presented in Table 1. The accuracy in terms of true positive and false positive volume fractions (TPVF and FPVF) [**Error! Bookmark not defined.**42], and average surface distance is shown. TPVF indicates the fraction of the total amount of tissue in the true delineation; FPVF denotes the amount of tissue falsely identified, which are defined as follows,

$$\mathrm{TPVF}=\frac{|C_{TP}|}{|C_{td}|}, \quad (15)$$

$$\text{FPVF}=\frac{|C_{FP}|}{|U_d - C_{td}|}. \quad (16)$$

Where, U_d is assumed to be a binary scene with all voxels in the scene domain set to have a value 1, and C_{td} is the set of voxels in the true delineation, $|\cdot|$ denotes volume. More details can be seen in [**Error! Bookmark not defined.**42].

3.3 Evaluation of Registration

Fig. 4 shows the registration results by the proposed method on three slices. We can see from it that our registration achieved very good results: the overlap is not good before the registration due to the large deformations, while after registration, two images overlap perfectly.

The alignment of regions of interests (ROIs) is a good indicator of how well two images are registered [51]. In this paper, the average relative overlap accuracy (AROA) is used for the quantitative evaluation of the registration method. The relative overlap of segmentations is a measure of how well two corresponding segmented regions agree with each other. Twenty ROIs have been selected by an imaging expert according to the following criteria: (i) wide distribution of ROIs throughout the CCT image and (ii) simple and accurate identification of all the ROIs. Fig. 5 shows some examples of selected ROIs. The AROA is computed based on all the ROIs as follows,

$$AROA=\frac{1}{N}\sum_{i=1}^{N}\frac{ROI_x(i)\cap ROI_y(i)}{ROI_x(i)\cup ROI_y(i)} \quad (17)$$

where $ROI_x(i)$ and $ROI_y(i)$ being the i^{th} corresponding ROI in the two images, and N is the number of ROIs.

Table 2 shows the influence of the standard deviation σ of the Gaussian kernel used during the demons registration process to the deformation field. Results showed that the best performance was reached for $\sigma = 3$ and this value was adopted in this paper.

Table 3 shows the influence of the number of iterations on the landmark mapping and on the CPU time. As expected, the CPU time increases linearly with the number of iterations. Beyond 50 iterations, the improvement in the accuracy is not significant anymore. This value was adopted for the experiments presented in this paper.

In terms of efficiency, the average computation time for the initialization, segmentation and registration on an Intel Xeon E5440 workstation with 2.83GHz CPU, 8 GB of RAM was 1, 1 and 10 minutes, respectively. The time for the ECV map computation is very little so it is neglected. The whole process is fast and acceptable for the clinical use.

3.4 Reproducibility Analysis of the Proposed Method

The proposed method consists of two steps: initialization and segmentation, in which the segmentation is fully automatic, however initialization step needs user interaction. So the reproducibility analysis was performed for the proposed method. User1 (XC) performed the proposed method (3D whole heart) twice and User2 (MN) performed the proposed method (3D whole heart) once. The same reproducibility analysis was performed to the manual method and the results were compared to the proposed method. Fig. 6 shows the linear regression analysis results of the proposed method vs manual on mean myocardium density. We can see from that the proposed 3D whole heart ECV method has much higher

reproducibility (R^2 is 0.963 and 0.961 for intra and inter, respectively) than the manual method (R^2 is 0.917 and 0,900 for intra and inter, respectively).

3.5 Statistical Correlation Analysis of the ECV value between Manual and the Proposed Method

In this section, we will focus on the ECV value comparison.In clinical settings, ECV is typically measured using several 2D ROIs. CCT data was first reformatted to the short axis plane to correspond to the CMRI acquisition, then myocardial and blood pool attenuation values at the base, mid and apex were measured twice and the average value was used as manual result for analysis. It is important to notice that, the manual result here is different from the manual result which is 3D manual segmentation result and used for the reproducibility analysis. Here the statistical correlation analysis between the proposed method and manual was performed. The linear regression analysis and Pearson's correlation were used to examine the relationship between automated and manual results. The Bland-Altman method was also used to calculate the bias and limits of agreement. P-values <0.05 were considered to be statistically significant.

Figs. 7 and 8 show the linear regression and Bland-Altman analysis results of mean myocardium and blood pool density obtained by manual and the proposed method. We can see the proposed method achieved high correlation with the manual results on myocardium and blood pool density. As the ECV value is computed based on the myocardium and blood pool intensity, it is nature to find that they are highly correlated. Fig. 9 shows the differentiation between normal and heart failure groups using ECV value by manual and the proposed method (3D whole heart). We can see from that similar to the manual analysis, the proposed method can differentiate the normal and heart failure group. Fig. 10 shows the visualization results of 3D ECV map on normal and heart failure subjects. We can find that the heart failure subject has much higher ECV values for most voxels than normal subject.

IV. DISCUSSIONS AND CONCLUSIONS

In this paper, we proposed a framework for the 3D whole heart ECV estimation for low dose CCT images. The proposed framework consists of three main steps: (1) myocardium and blood pool segmentation based on shape constrained GC method; (2) pre and post-contrast cardiac images registration based on symmetric Demons algorithm; and (3) ECV value computation. The proposed method was tested on 20 clinical low dose CCT datasets with pre-contrast and post-contrast images. The preliminary results show that: (1) The good segmentation and registration performance demonstrated the feasibility and efficiency of the proposed method. (2) The proposed method achieved high correlations with manual analysis results. (3) The proposed method has much higher reproducibility than manual method.

Here we investigated a semi-automatic 3D ECV estimation method based on two CCT phases: pre-contrast and post-contrast. Compared to the three phase (as shown in Fig. 11) method, two CCT scans results in less radiation exposure for the patient. And another issue is CT angiography image generally acquired at different phase compared with CCT pre- and post-contrast phases. However, when the CT angiography scan is used, the blood pool can be easily segmented by threshold method (see Fig. 11 (b)) and then this blood pool can be used as a shape constraint for myocardium segmentation based on the shape constrained GC method, which makes the whole framework fully automatic. The fully automatic framework will be investigated in the near future.

In the clinical environment, CMRI has been validated for detection of myocardial fibrosis, in which ECV fraction was used as an important factor. However, for CMRI, the ECV fraction was usually computed based on several 2D ROIs. In this paper, we computed the 3D whole

heart ECV fraction based on the low dose CCT images. The statistical analysis was performed between the proposed method and manual ECV analysis results. We find from the results that the proposed method achieved high correlation with the manual results. However, the proposed method was tested on only 20 CCT images. The proposed method will be tested on more data set in the near future.

Acknowledgments

This research was supported in part by the Intramural Research Program of the Clinical Center, NIH.

References

[1]. Schelbert EB, Testa SM, Meier CG, et al. Myocardial extravascular extracellular volume fraction measurement by gadolinium cardiovascular magnetic resonance in humans: slow infusion versus bolus. Journal of cardiovascular magnetic resonance: official journal of the Society for Cardiovascular Magnetic Resonance. 2011; 13:16. [PubMed: 21375743]

[2]. Flett AS, Hayward MP, Ashworth MT, et al. Equilibrium contrast cardiovascular magnetic resonance for the measurement of diffuse myocardial fibrosis: preliminary validation in humans. Circulation. 2010; 122:138–44. [PubMed: 20585010]

[3]. Hundley WG, Bluemke DA, Finn JP, et al. ACCF/ACR/AHA/NASCI/SCMR 2010 expert consensus document on cardiovascular magnetic resonance: a report of the American College of Cardiology Foundation Task Force on Expert Consensus Documents. Circulation. 2010; 121(22): 2462–508. [PubMed: 20479157]

[4]. Sibley C, Huang J, Ugander M, et al. Myocardial and blood T1 quantification in normal volunteers at 3T. Journal of Cardiovascular Magnetic Resonance. 2011; 13:P51.

[5]. Sparrow P, Messroghli DR, Reid S, Ridgway JP, Bainbridge G, Sivananthan MU. Myocardial T1 mapping for detection of left ventricular myocardial fibrosis in chronic aortic regurgitation: pilot study. AJR American journal of roentgenology. 2006; 187:W630–5. [PubMed: 17114517]

[6]. Heckbert SR, Post W, Pearson GD, et al. Traditional cardiovascular risk factors in relation to left ventricu lar mass, volume, and systolic function by cardiac magnetic resonance imaging: the Multiethnic Study of Atherosclerosis. J Am Coll Cardiol. 2006; 48:2285–92. [PubMed: 17161261]

[7]. Senra T, Shiozaki AA, Salemi VM, Rochitte CE. Delayed enhancement by multidetector computed tomography in endomyocardial fibrosis. European Heart Journal. 2008; 329:347. [PubMed: 17827498]

[8]. Craciunescu O, Brizel D, Cleland E, Yoo D, Muradyan N, Carroll M, Barboriak D, MacFall J. Dynamic contrast enhanced-MRI in head and neck cancer patients: variability of the precontrast longitudinal relaxation time (T10). Medical Physics. 2010; 37(6):2683–92. [PubMed: 20632579]

[9]. Petitjean C, Dacher J-N. A review of segmentation methods in short-axis cardiac images Medical Image Analysis. 2011; vol. 15:169–184.

[10]. Canny J. A computational approach to edge detection. IEEE Transactions on Pattern Analysis and Machine Intelligence. 1986; 8:769–798.

[11]. Deriche R. Using Canny's criteria to derive a recursively implemented optimal edge detector. International Journal of Computer Vision. 1987; 1:167–187.

[12]. Singh A, Kurowski L, Chiu M. Cardiac MR Image Segmentation Using Deformable Models. Proc. of SPIE – The International Society for Optical Engineering. 1993; 1905(8):8–28.

[13]. Kass M, Witkin A, Terzopoulos D. Snakes: Active contour models. International Journal of Computer Vision. 1988; 1:321–332.

[14]. Charnoz A, Lingrand D, Montagnat J. A levelset based method for segmenting the heart in 3D+T gated SPECT image. International Workshop on Functional Imaging and Modeling of the Heart. 2003; 2674 DOI: 10.1007/3-540-44883-7_6.

[15]. Udupa JK, Samarasekera S. Fuzzy connectedness and object definition: Theory, algorithms, and applications in image segmentation. Graphical Models and Image Processing. 1996; 58(3):246–261.

[16]. Boykov Y, Kolmogorov V. An Experimental Comparison of Min-Cut/Max-Flow Algorithms. IEEE Trans. Pattern Analysis and Machine Intelligence. 2004; 26(9):1124–1137.

[17]. Nastar C, Ayache N. Frequency-based nonrigid motion analysis: Application to four dimensional medical images. IEEETransactions on Pattern Analysis and Machine Intelligence. 1996; 18(11): 1067–1079.

[18]. Park J, Metaxas D, Axel L. Analysis of left ventricular motion based on volumetric deformable models and MRISPAMM. Medical Image Analysis. 1996; 1(1):53–71. [PubMed: 9873921]

[19]. Gerard O, Collet-Billon A, Rouet J-M, Jacob M, Fradkin M, Allouche C. Efficient model-based quantification of left ventricle function in 3D echocardiography. IEEE Transaction in Medical Imaging. 2002; 21(9):1059–1068.

[20]. Sermesant, M.; Coudiere, Y.; Delingette, H.; Ayache, N. Progress towards an electro-mechanical model of the heart for cardiac image analysis. IEEE International Symposium on Biomedical Imaging; 2002. p. 10-13.

[21]. Chandrashekara, R.; Rao, A.; Sanchez-Ortiz, GI.; Mohiaddin, RH.; Rueckert, D. Construction of a statistical model for cardiac motion analysis using non-rigid image registration. Proceedings of the 18th International Conference On Information Processing in Medical Imaging; 2003. p. 599-610.

[22]. Frangi AF, Rueckert D, Schnabel JA, Niessen WJ. Automatic construction of multiple object three-dimensional statistical shape models: Application to cardiac modeling. IEEE Transactions on Medical Imaging. 2002; 21(9):1151–1166. [PubMed: 12564883]

[23]. Üzümcü, M.; Frangi, AF.; Sonka, M.; Reiber, JHC.; Lelieveldt, BPF. Medical Image Computing and Computer-Assisted Intervention. 2001. Ica vs. pca active appearance models: Application to cardiac MR segmentation; p. 451-458.

[24]. Zheng Y, Barbu A, Georgescu B, Scheuering Michael, Comaniciu D. Four-Chamber Heart Modeling and Automatic Segmentation for 3D Cardiac CT Volumes Using Marginal Space Learning and Steerable Features. IEEE Transactions on Medical Imaging. 2008; Vol. 27(No. 11): 1668–1681. [PubMed: 18955181]

[25]. Lin, X.; Cowan, B.; Young, A. Model-based Graph Cut Method for Segmentation of the Left Ventricle. Conference Proceedings of the International Conference of IEEE Engineering in Medicine and Biology Society; 2005. p. 3059-3062.

[26]. Suri, J. Segmentation and Quantification Techniques for Fitting Computer Vision Models to Cardiac MR, CT, C-Ray and PET Image Data. In: Suri, J.; Setarehdan, S.; Singh, S., editors. Advanced Algorithmic Approaches to Medical Image Segmentation. 2002. p. 131-227.

[27]. Malcolm JJ, Rathi YY, Tannenbaum AA. Graph Cut Segmentation with Nonlinear Shape Priors. Proceedings of the IEEE International Conference on Image Processing. 2007; IV:365–368.

[28]. Vu, N.; Manjunath, BS. Shape Prior Segmentation of Multiple Objects with Graph Cuts. Proceedings of the 2008 IEEE Computer Society Conference on Computer Vision and Pattern Recognition; 2008. p. 1-8.

[29]. Daniel, Cremers; Stanley, J. Osher and Stefano Soatto, Kernel Density Estimation and Intrinsic Alignment for Shape Priors in Level Set Segmentation. International Journal of Computer Vision. 2006; 69(3):335–351.

[30]. Chan, T.; Zhu, W. Computational Applied Mathematics. UCLA; Los Angeles: 2003. Level set based shape prior segmentation, Technical Report 03-66.

[31]. Wirth, MA.; Choi, C.; Jennings, A. Point-to-point registration of nonrigid medical images using local elastic transformation methods. IEEE Int. Conf. Image Processing and Its Applications; 1997. p. 780-784.

[32]. Mäkelä, TH.; Clarysse, P.; Lötjönen, J.; Sipilä, O.; Lauerma, K.; Hänninen, H.; Pyökkimies, E-P.; Nenonen, J.; Knuuti, J.; Katila, T.; Magnin, IE. Lecture Notes in Computer Science 2208: Medical Image Computing and Computer-Assisted Intervention. 2001. A new method for the registration of cardiac PET and MR images using deformable model based segmentation of the main thorax structures; p. 557-564.

[33]. Audette MA, Ferrie FP, Peters TM. An algorithmic overview of surface registration techniques for medical imaging. Medical image Analysis. 2000; 4:201–217. [PubMed: 11145309]

[34]. Dey D, Slomka PJ, Hahn LJ, Kloiber R. Automatic threedimensional multimodality registration using radionuclide transmission CT attenuation maps: A phantom study. J. Nucl. Med. 1999; 40(3):448–455. [PubMed: 10086710]

[35]. Wan, R.; Li, M. An Overview of Medical Image Registration. Proceedings of the Fifth International Conference on Computational Intelligence and Multimedia Applications; 2003. p. 385-390.

[36]. Klein GJ, Reutter NW, Huesman RH. Four-dimensional affine registration models for respiratory-gated PET. IEEE Transactions on Medical Imaging. 2002; 48:756–760.

[37]. Hatak NS, Maas SA, et al. Strain measurement in the left ventricle during systole with deformable image registration. Medical Image Analysis. 2009; 13(2):354–361. [PubMed: 18948056]

[38]. Vemuri BC, Ye J, Chen Y, Leonard CM. Image registration via level-set motion: Applications to atlasbased segmentation. Medical Image Analysis. 2003; 7:1–20. [PubMed: 12467719]

[39]. Wells WM, Viola P, Atsumi H, Nakajima S, Kikinis R. Multi-modal volume registration by maximization of mutual information. Medical Image Analysis. 1996; 1(1):35–51. [PubMed: 9873920]

[40]. Josien PW, Pluim JB, Antoine Ma, Viergever MA. Mutual information based registration of medical images: a survey. IEEE Transactions on Medical Imaging. 2003; 22(8):986–1004. [PubMed: 12906253]

[41]. Vercauteren TX, Pennec, et al. Diffeomorphic demons: Efficient non-parametric image registration. NeuroImage. 2009; 45:S61–S72. [PubMed: 19041946]

[42]. Thirion JP. Image matching as a diffusion process: An analogy with Maxwell's demons. Medical Image Analysis. 1998; 2(3):243–260. [PubMed: 9873902]

[43]. Wang H, Dong L, O'Daniel J, Mohan R, Garden AS, Ang KK, Kuban DA, Bonnen M, Chang JY, Cheung R. Validation of an accelerated 'demons' algorithm for deformable image registration in radiation therapy. Physics in Medicine and Biology. 2005; vol. 50(no. 12)

[44]. Vercauteren, Tom; Pennec, Xavier; Perchant, Aymeric; Ayache, Nicholas. Symmetric Log-Domain Diffeomorphic Registration: A Demons-based Approach. Proceedings of the 11th International Conference on Medical Image Computing and Computer Assisted Intervention (MICCAI 2008); New York, NY. September 6 - 10 2008;

[45]. Vercauteren, Tom; Pennec, Xavier; Malis, Ezio; Perchant, Aymeric; Ayache, Nicholas. Insight Into Efficient Image Registration Techniques and the Demons Algorithm. Information Processing in Medical Imaging. 2007; 4584/2007:495–506. [PubMed: 17633724]

[46]. Falcao AX, Udupa JK, Samarasekera S, Sharma S. User-Steered Image Segmentation Paradigms: Live Wire and Live Lane. Graphical Models and Image Processing. 1998; 60:233–260.

[47]. Kolmogorov V, Zabih R. What Energy Functions can be Minimized via Graph Cuts? IEEE Transactions on Pattern Analysis and Machine Intelligence. 2004; 26(2):147–159. [PubMed: 15376891]

[48]. Ciesielski KC, Chen X, Udupa JK, Grevera GJ. Linear time algorithms for exact distance transform. Journal of Mathematical Imaging and Vision. 2011; 39(3):193–209.

[49]. Insight Segmentation and Registration Toolkit (ITK). http://www.itk.org/

[50]. Udupa JK, Leblanc VR, Zhuge Y, Imielinska C, Schmidt H, Currie LM, Hirsch BE, Woodburn J. A framework for evaluating image segmentation algorithms. Computerized Medical Imaging and Graphics. 2006; 30(2):75–87. [PubMed: 16584976]

[51]. Fitzpatrick JM, Hill DLG, Shyr Y, West J, Studholme C, Maurer CR. Visual assessment of the accuracy of retrospective registration of MR and CT images of the brain. IEEE Transactions on Medical Imaging. 1998; 17(4):571–585. [PubMed: 9845313]

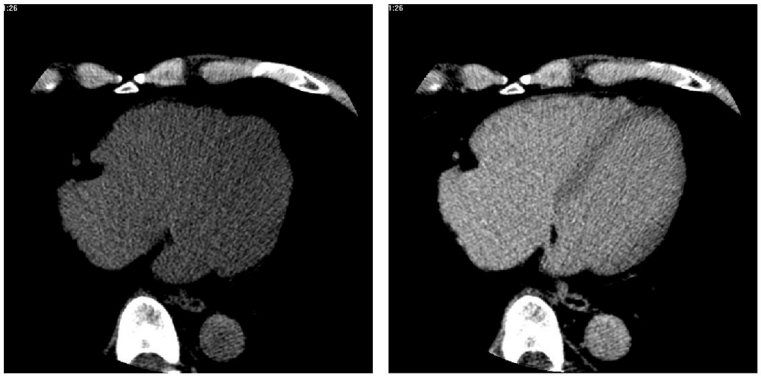

(a) (b)

Fig. 1.
Examples of two phases of CCT: (a) pre-contrast; (b) post-contrast.

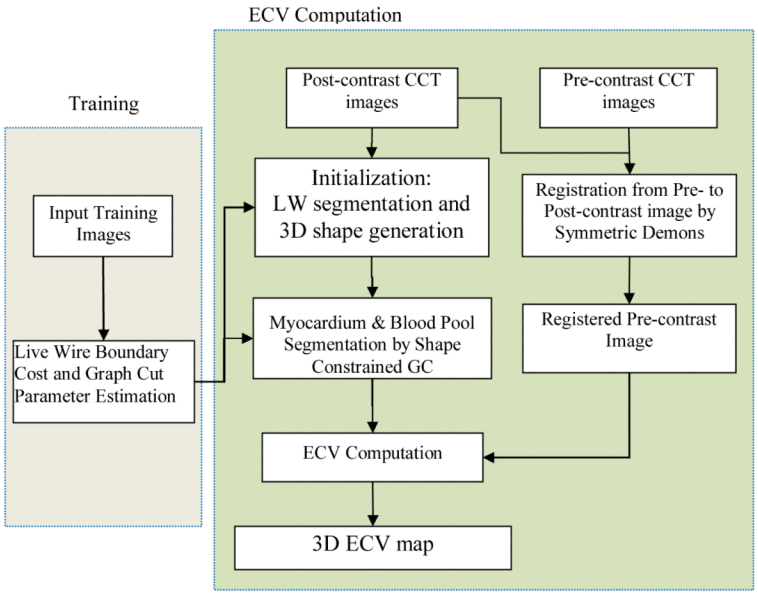

Fig. 2.
The flowchart of the proposed method.

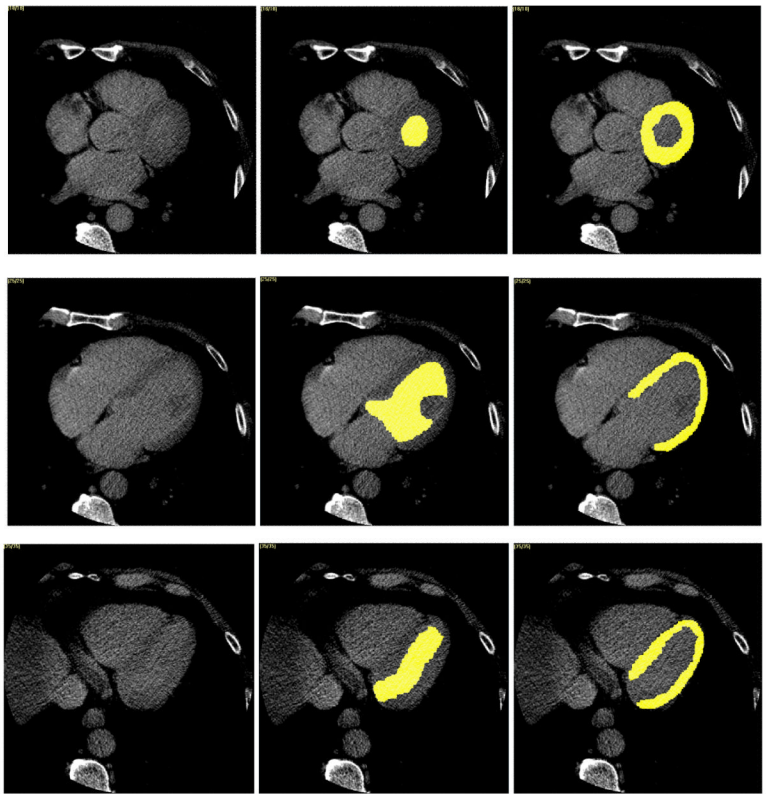

Fig. 3.
Myocardium and blood pool segmentation results by the proposed shape constrained GC method on one patient's post contrast-enhanced image - three slices. (a) original image; (b) blood pool segmentation result; (c) myocardium segmentation result.

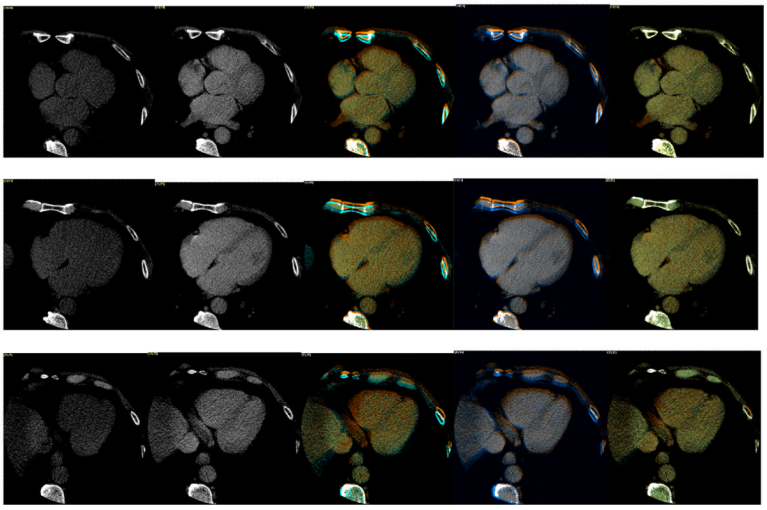

Fig. 4.

Symmetric Demons Registration Results on one patient's three slices. The first column shows the pre-contrast image; the second shows the post-contrast image; the third column shows the overlap of the pre-contrast (cyan color) over the post-contrast image (orange color); the fourth column shows the overlap of the registered pre-contrast (blue color) using affine registration over the post-contrast image (orange color); and the last column shows the overlap of registered pre-contrast (cyan color) by the symmetric forces demons over the post-contrast image (orange color).

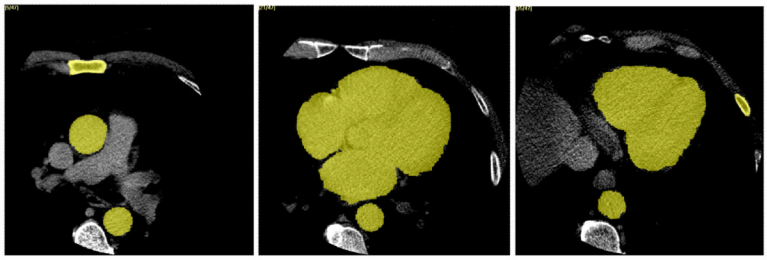

Fig. 5.
Examples of selected ROIs.

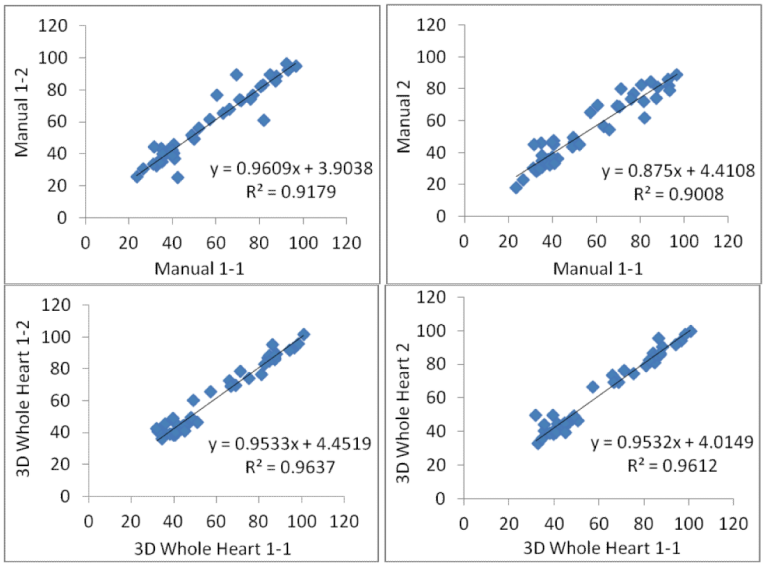

Fig. 6.
Reproducibility analysis results of the proposed method vs manual on mean myocardium density (HU).

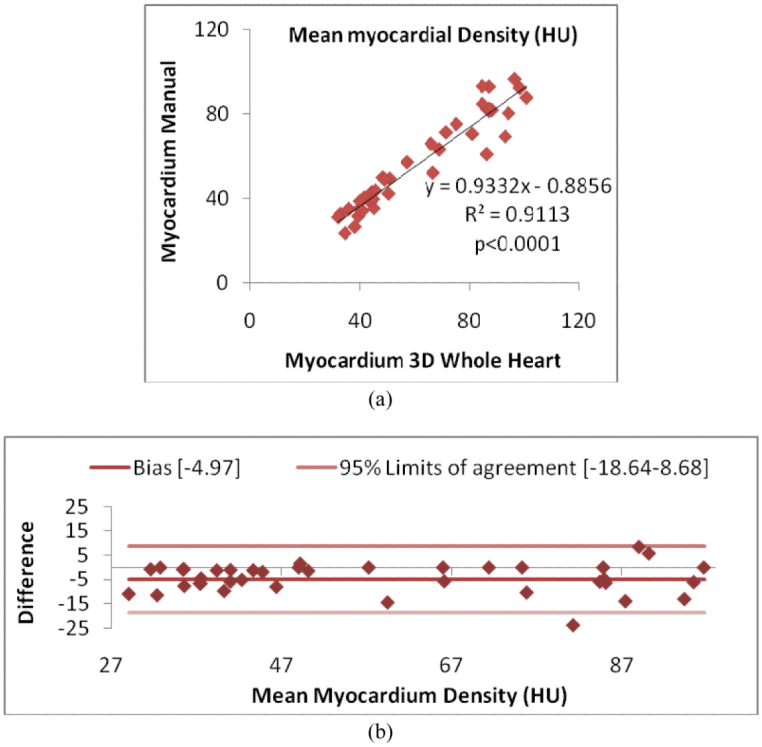

Fig. 7.

Results of mean myocardium density obtained by manual and the proposed method (3D whole heart). (a) Linear regression analysis and (b) Bland-Altman analysis.

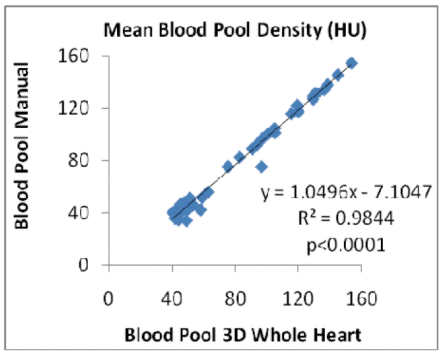

(a)

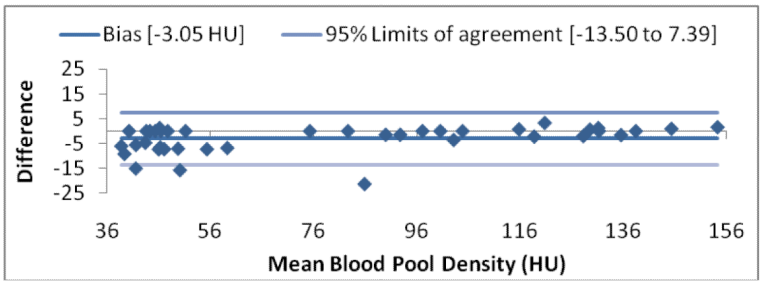

(b)

Fig. 8.

Results of mean blood pool density obtained by manual and the proposed method (3D whole heart). (a) Linear regression analysis and (b) Bland-Altman analysis.

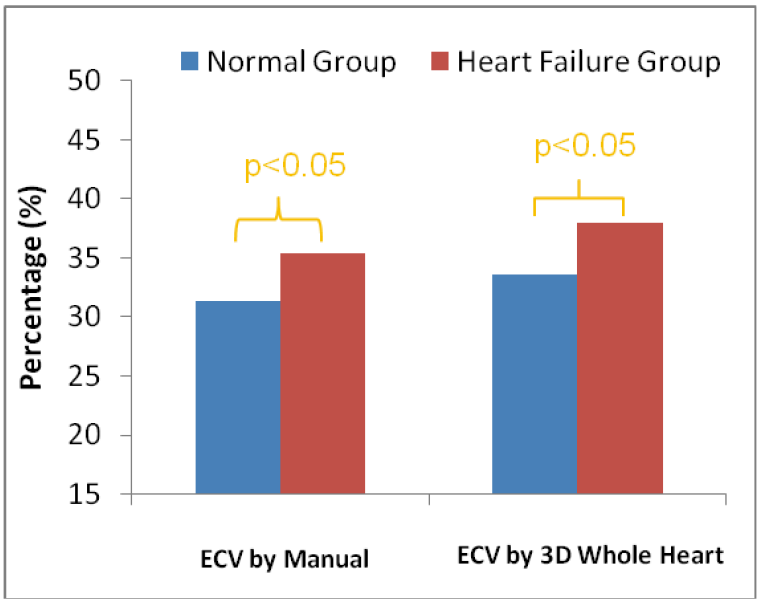

Fig. 9.
Differentiation between normal and heart failure groups using ECV by manual and the proposed method (3D whole heart).

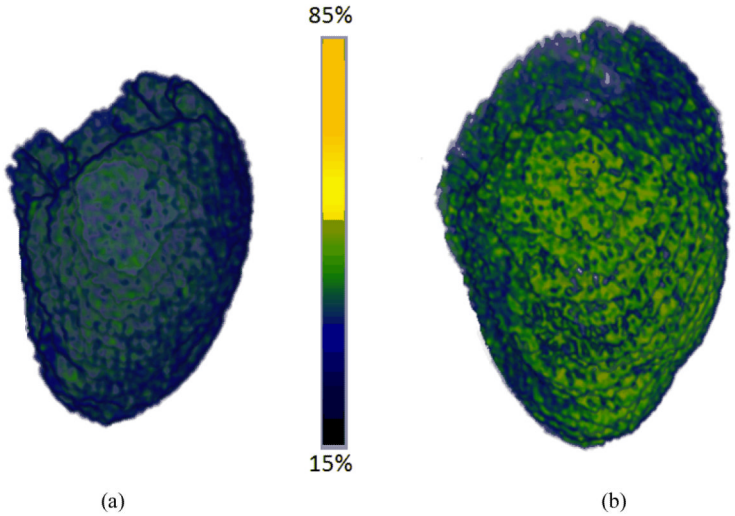

Fig. 10.
The visualization of 3D CCT ECV map on two subjects. (a) Normal subject; (b) Heart failure subject. The heart failure subject has much higher ECV values for most voxels than normal subject.

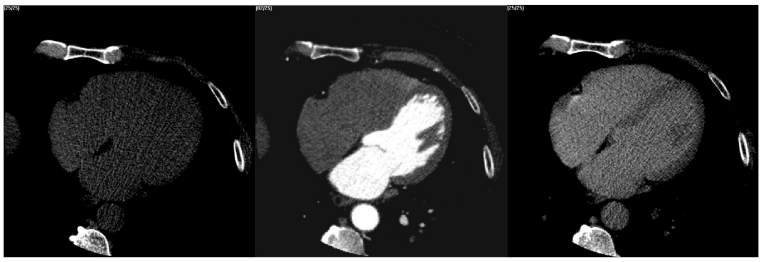

(a) (b) (c)

Fig. 11.
Three phases cardiac CT images. (a) Pre-contrast image; (b) CT angiography image; (c) Post-contrast Image.

Table 1

Mean and standard deviation of TPVF, FPVF and Average Surface Distance for the proposed method on post-contrast image.

	TPVF (%)	FPVF (%)	Average Surface Dist (mm)
Myocardium	92.2 ±1.5	0.66 ±0.12	0.72 ±0.39
Blood Pool	93.2 ±1.1	0.52 ±0.09	0.66 ±0.31

Table 2

The influence of the standard deviation σ of the Gaussian kernel on landmark mapping.

Σ	0.5	1	2	3	4	5
AROA(%)	84.6	89.2	89.6	90.3	90.2	90.1

Table 3

The influence of the number of iterations on the landmark mapping and on the CPU time ($\sigma = 3$).

Number of iterations	*AROA* (%)	CPU time (min.)
10	84.1	2.2
20	87.9	3.8
50	90.3	10.0
80	90.4	14.5
100	90.5	18.2